

> REPLACE THIS LINE WITH YOUR MANUSCRIPT ID NUMBER (DOUBLE-CLICK HERE TO EDIT) <

A 50THz Ultra-Wideband Nano-Photonics Perfect Absorber Biosensor for Label-Free Detection of Circulating Cancer Exosomes: Advancing Early Cancer Diagnostics

Musa N. Hamza, Mohammad Tariqul Islam, Sunil Lavadiya, Iftikhar ud Din, Bruno Sanches, Slawomir Koziel, Syeda Iffat Naqvi, Abinash Panda, Mohammad Alibakhshikenari, Bal Virdee, D. Mariyanayagam, R. Jayanthi, S. Fernando and Md. Shabiul Islam

Abstract— This paper addresses the challenge of early-stage cancer diagnosis using microwave imaging (MWI) techniques by targeting circulating exosomes, recently identified as promising cancer biomarkers. We introduce an innovative nano-photonics perfect absorber (NPA) operating in the terahertz (THz) range, offering a significant improvement over existing MWI-based approaches in terms of simplicity, sensitivity, and specificity. Unlike previous THz absorbers, the proposed NPA achieves an exceptionally wide operating bandwidth from 100 GHz to 50 THz with an absorption efficiency exceeding 97.5%, while featuring an ultra-compact nanoscale footprint (100 × 100 nm², thickness 30 nm). The design integrates a silver (Ag) resonator and a nickel (Ni) ground plane on a silicon dioxide (SiO₂) substrate, with meticulously tuned geometries to create multiple resonance modes, enabling continuous broadband absorption. Full-wave electromagnetic simulations validate the structure's performance, including electric and magnetic field distributions, surface currents, and scattering parameters. Comparative analysis with state-of-the-art absorbers demonstrates the superior bandwidth, absorption stability, and angular robustness of our device. Furthermore, we demonstrate the NPA's unique ability to act as a label-free biosensor for exosome detection, where cancerous exosomes consistently induce stronger electric field responses than normal exosomes due to their distinct molecular compositions. These results confirm the proposed NPA as a novel, highly effective platform for non-invasive, early-stage cancer diagnostics via MWI.

Index Terms— Nano-Photonic Perfect Absorber (NPA); Terahertz (THz) Imaging; Label-Free Exosome Detection; Ultra-Wideband Absorber; Early Cancer Diagnostics

I. INTRODUCTION

Cancer remains a significant global health challenge, with the World Health Organization and other agencies projecting a concerning rise in cancer incidence and mortality rates in the coming years. By 2030, it is estimated that there will be 17 million cancer-related deaths and 26 million new diagnoses worldwide [1], driven by factors such as population growth, aging, lifestyle changes, and environmental exposures [2]. Efforts to counter these projections focus on advancing early detection, improving access to treatments, and investing in innovative therapies such as targeted treatments, immunotherapy, and gene therapy [3].

Early detection plays a critical role in improving patient outcomes by enabling timely interventions, increasing survival rates, and reducing treatment-related morbidity. Recent advances in diagnostic technologies including liquid biopsy, nano-photonics, multi-omics approaches, and microfluidics platforms—have accelerated the development of highly sensitive and minimally invasive cancer detection strategies [4], [5].

Among emerging biomarkers, circulating cancer exosomes have gained particular attention. These extracellular vesicles (30–150 nm in diameter) are released by cancer cells into the

The authors gratefully acknowledge the financial support of the University of Doha for Science and Technology under Grant No. KK-2024-005. Additionally, part of this research has been supported by the Icelandic Research Fund (Grant No. 239858), by the National Science Centre of Poland (Grant No. 2020/37/B/ST7/01448). (Corresponding authors: Musa N. Hamza ; Mohammad Tariqul Islam; Mohammad Alibakhshikenari; Md. Shabiul Islam)

Musa N. Hamza is with Department of Physics, College of Science, University of Raparin, Sulaymaniyah 46012, Iraq. (e-mail: musa.nuraden@uor.edu.krd)

Mohammad Tariqul Islam is with Department of Electrical, Electronic and Systems Engineering, Faculty of Engineering and Built Environment, Universiti Kebangsaan Malaysia, 43600 UKM Bangi, Selangor, Malaysia. (e-mail: tariqul@ukm.edu.my)

Sunil Lavadiya is with Department of Information and Communication Technology, Marwadi University, Rajkot-360003, Gujarat, India. (e-mail: sunil.lavadiya@marwadieducation.edu.in)

Iftikhar ud Din is with Telecommunication Engineering Department, University of Engineering and Technology, Mardan 23200, Pakistan. (e-mail: iftikharuddin114@gmail.com)

Bruno Sanches is with Department of Electronic Systems Engineering, Escola Politécnica da Universidade de São Paulo São Paulo, Brazil. (e-mail: bruno.csanches@usp.br)

Slawomir Koziel is with Engineering Optimization & Modeling Center, Reykjavik University, 102 Reykjavik, Iceland. He is also with the Faculty of Electronics, Telecommunications and Informatics, Gdansk University of Technology, 80-233 Gdansk, Poland. (e-mail: Koziel@ru.is)

Syeda Iffat Naqvi is with Department of Telecommunication Engineering University of Engineering & Technology Taxila, Pakistan. (e-mail: iffat.naqvi@uettaxila.edu.pk)

Abinash Panda is with Department of Electronics and Communication Engineering, CMR Institute of Technology, Bengaluru 560037, India. (e-mail: abinashpanda087@gmail.com)

Mohammad Alibakhshikenari is with the Electronics Engineering Department, University of Rome "Tor Vergata", 00133 Rome, Italy. He is also with the Department of Electrical and Electronics Engineering, Dogus University, 34775 Umraniye, Istanbul, Türkiye. (e-mail: alibakhshikenari@ing.uniroma2.it)

Bal Virdee, D. Mariyanayagam, R. Jayanthi, and S. Fernando are with Department of Center for Communications Technology, London Metropolitan University, London N7 8DB, United Kingdom; (e-mail: b.virdee@londonmet.ac.uk, d.mariyanayagam@londonmet.ac.uk, r.rajaguruJayanthi1@londonmet.ac.uk, s.fernando@londonmet.ac.uk)

Md. Shabiul Islam is with Centre for Advanced Devices and Systems, Faculty of Artificial Intelligence and Engineering, Multimedia University, Persiaran Multimedia, 63100 Cyberjaya, Selangor, Malaysia. (e-mail: shabiul.islam@mmu.edu.my)

> REPLACE THIS LINE WITH YOUR MANUSCRIPT ID NUMBER (DOUBLE-CLICK HERE TO EDIT) <

bloodstream and carry diverse biomolecules—proteins, lipids, DNA, RNA, and microRNAs—that reflect the molecular signature of their parent cells [6]. Circulating exosomes are crucial mediators of tumor progression, metastasis, and immune evasion, making them valuable targets for liquid biopsy applications. Notably, changes in the quantity and molecular composition of exosomes can precede the detection of tumors by conventional imaging methods, positioning them as promising biomarkers for early-stage cancer diagnosis [7], [8].

Traditional exosome detection techniques often rely on labeling strategies involving antibodies or dyes. While effective, these methods are typically labor-intensive, expensive, and susceptible to non-specific binding, which can compromise detection accuracy. In this context, label-free detection technologies offer significant advantages by simplifying sample preparation and reducing false positives.

Nano-photonic perfect absorbers (NPAs) represent a powerful, label-free sensing approach that leverages near-total absorption of specific light wavelengths to enhance sensitivity and specificity [9]. NPAs are engineered using metamaterials, plasmonic nanostructures, or photonic crystals that manipulate light at sub-wavelength scales [10], [11]. These structures are tunable to achieve optimal absorption at designated frequencies, making them highly suitable for sensing applications. In comparison to conventional techniques such as ELISA, NPA-based sensors enable faster, real-time detection by directly monitoring optical property changes as exosomes bind to the sensor surface. This approach not only enhances detection sensitivity at low concentrations—critical for early cancer diagnosis—but also allows non-invasive sampling through body fluids like blood, urine, or saliva [12]–[14].

Recent research has extended the use of nano-photonic absorbers across a range of electromagnetic frequencies, from the gigahertz (GHz) to terahertz (THz) and even petahertz (PHz) regimes [15]–[52]. Significant progress has been made in the THz domain, where unique interaction with biomolecular structures enables non-invasive, high-specificity sensing. Studies such as Xiaolong et al. [53], Cheng et al. [54], and others [55], [56] have demonstrated various THz absorbers with enhanced bandwidth, multi-band functionality, and tunability for biomedical applications. However, many existing designs face limitations in terms of operational bandwidth, sensitivity, angular stability, or fabrication complexity.

Building on these advancements, this study introduces a novel ultra-wideband nano-photonic perfect absorber specifically tailored for label-free detection of circulating cancer exosomes. Operating from 0.1 THz to 50 THz with an impressive 97.5% absorption efficiency, the proposed NPA utilizes a hybrid structure of silver (Ag) resonators and a nickel (Ni) ground plane on a silicon dioxide (SiO₂) substrate. Advanced resonator geometries and full-wave electromagnetic simulation methods validate the design's broadband, high-sensitivity performance.

The THz spectral region offers distinct advantages for biological diagnostics, being non-ionizing and safe for imaging soft tissues [60]. It enables detailed visualization of biological structures and hydration levels, supporting early cancer detection, tissue monitoring, and real-time therapeutic evaluation [15]–[20], [22]–[34], [36]–[39]. Integrating high-efficiency THz absorbers within sensing platforms enhances

signal-to-noise ratios by minimizing reflections and transmission losses, thereby improving imaging and detection reliability [61], [62].

Although NPAs hold transformative potential, challenges remain in achieving selective, stable surface functionalization for exosome detection and in ensuring reproducible, scalable fabrication processes. Addressing these issues requires interdisciplinary advances in nanofabrication, surface chemistry, and system integration.

This research presents a novel terahertz nano-photonic perfect absorber offering significant improvements in bandwidth, sensitivity, and label-free biosensing capability. By enabling highly sensitive detection of cancerous exosomes through non-invasive methods, the proposed NPA offers a promising route toward earlier, more accurate cancer diagnostics.

The remainder of this paper is organized as follows. Section II presents the structural design of the nano-photonic absorber and discusses the electromagnetic field alignment. Section III analyzes the absorption characteristics and provides a comparative study with existing designs. Section IV focuses on the nano-photonic structure design and parameter optimization. Section V examines the electric and magnetic field distributions as well as surface current analysis. Section VI investigates the detection and diagnosis of circulating cancer exosomes. Section VII benchmarks the proposed absorber against state-of-the-art devices. Section VIII discusses the experimental limitations and outlines future validation strategies. Section IX offers a future perspective on the development and application of technology. Finally, Section X concludes the paper with a summary of the key findings and contributions.

II. STRUCTURAL DESIGN AND ELECTROMAGNETIC FIELD ALIGNMENT

This work presents a modified metal-insulator-metal (MIM) nano-photonic perfect absorber, specifically engineered to maximize terahertz (THz) absorption across an ultra-wide frequency range for biomedical diagnostics, with particular emphasis on cancer-related exosome detection. The absorber employs a dual-metal configuration: a silver (Ag) front layer and a nickel (Ni) ground plane, arranged into distinct resonant structures. By optimizing electromagnetic (EM) field alignment at the nanoscale, the design achieves both broad spectral absorption and high sensitivity.

A. Structural Design

The front layer integrates three primary silver-based resonators, as illustrated in Figure 1. The first two resonators (Figures 1(a) and 1(b)) feature wide-cross geometries, inspired by interwoven metallic resonators, which initiate broad resonant responses in the lower THz region. A third resonator, a ring-shaped structure (Figure 1(c)), provides additional tunability and strengthens multi-band absorption by supporting localized surface plasmon modes.

Precise geometric parameters for these resonators are listed in Table 1, enabling fine control over their resonance frequencies and optimizing the absorber's performance across the targeted 100 GHz–50 THz range.

> REPLACE THIS LINE WITH YOUR MANUSCRIPT ID NUMBER (DOUBLE-CLICK HERE TO EDIT) <

The rear plane, depicted in Figure 2, consists of complementary nickel-based structures that enhance coupling and energy dissipation. The outer design (Figure 2(a)) uses a split-ring configuration to intensify magnetic field localization and improve impedance matching with free space. Central elements (Figures 2(b) and 2(c)) incorporate a disk and a ring resonator, which maintain effective surface current distribution and further support the absorber's broadband behavior.

The synergistic interaction between the front and rear resonators facilitates multi-resonant coupling, generating slightly shifted but overlapping resonance modes that produce continuous ultra-wideband absorption. This effect is critical for biosensing applications, where high sensitivity to minor dielectric environment changes is essential.

Furthermore, the carefully engineered geometries promote strong localization of both electric and magnetic fields around the resonators, resulting in efficient field confinement and energy trapping at the nanoscale. These properties collectively enhance the biosensor's ability to detect biomolecular targets, such as cancer-derived exosomes, with high sensitivity and specificity.

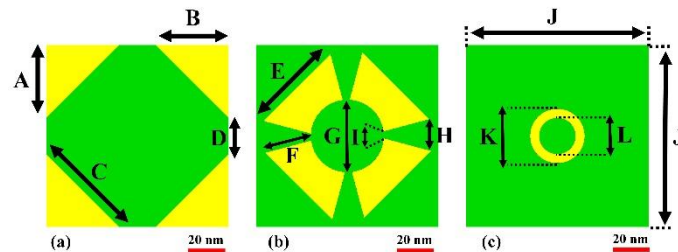


Figure 1: Schematic of the proposed nano-photonic perfect absorber, showing the front silver resonator layouts: (a) First resonator configuration, (b) Second resonator arrangement, (c) Third resonator design.

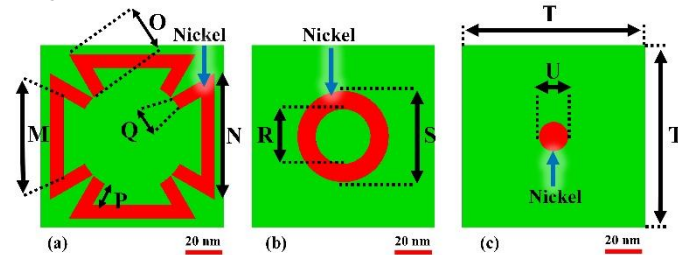


Figure 2: Schematic of the rear view of the nano-photonic absorber, highlighting the nickel ground plane structures: (a) Primary split-ring design, (b) Central ring structure, (c) Central disk structure.

B. Simulation and Design Optimization

The full-wave electromagnetic simulations were conducted using CST Studio Suite, a leading platform for high-frequency device modeling. To model open-space behavior accurately, Perfectly Matched Layers (PML) were implemented along the propagation direction (z -axis) to absorb outgoing waves and eliminate reflection artifacts at the simulation boundaries. Periodic boundary conditions were applied along the transverse (x and y) directions, effectively replicating an infinite array of the nano-photonic absorber's unit cell and enabling investigation of its collective optical response without edge effects.

A linearly polarized plane wave was used as the excitation source, with the electric field (E -field) aligned along the x -axis, the magnetic field (H -field) along the y -axis, and the wave vector (k) propagating along the negative z -axis, ensuring normal incidence onto the absorber surface. This setup mimics typical biosensing conditions, where vertical incidence is preferred.

TABLE 1: OPTIMIZED VARIABLE DIMENSIONS OF THE NANO-PHOTONICS ABSORBER

ABSORBER			
Parameters	Value (nm)	Parameters	Value (nm)
A	40	M	43.3
B	40	N	69.28
C	56.57	O	27.24
D	20	P	13.3
E	51.96	Q	7.56
F	26.02	R	30
G	39.82	S	50
H	17.5	T	100
I	3.77	U	16
J	100	SiO ₂ Thick	20
K	30	Ni Thick	5
L	20	Ag Thick	5

To capture nanoscale features with high fidelity, a highly refined adaptive mesh was employed, with particular focus on the intricate geometries of the silver and nickel resonators. A large simulation domain was also adopted to minimize near-field boundary effects and improve far-field absorption predictions.

Frequency-dependent material parameters for silver (Ag), nickel (Ni), and silicon dioxide (SiO₂) were incorporated, using experimentally measured permittivity and conductivity values to ensure physical realism across the 0.1–50 THz range.

Careful selection of wave source parameters guaranteed uniform illumination and precise polarization control, critical for evaluating the absorber's optical response. Symmetry planes were applied where appropriate to reduce computational cost while preserving simulation accuracy. Advanced post-processing techniques were used to extract absorption spectra, electric and magnetic field distributions, surface current densities, and scattering parameters (S -parameters), essential for optimizing the absorber design for label-free biosensing applications in early-stage cancer diagnostics.

The silicon dioxide layer was modeled with a relative permittivity (ϵ_r) of 3.9 and was treated as lossless (loss tangent = 0), considering that high-purity SiO₂ exhibits negligible dielectric loss across the terahertz frequency spectrum. This assumption enhances simulation efficiency without compromising accuracy.

C. Nano-Photonic Absorber for THz Biosensing

Nano-photonic absorbers operating in the terahertz (THz) regime offer significant advantages for biosensing applications due to their ability to support strong resonance phenomena at subwavelength scales. By leveraging materials with distinct dielectric or metallic properties, these structures achieve high absorption efficiency and strong field confinement, both critical for sensitive detection. Furthermore, the absorber's geometry, material composition, and surface functionalization with

> REPLACE THIS LINE WITH YOUR MANUSCRIPT ID NUMBER (DOUBLE-CLICK HERE TO EDIT) <

specific biomolecular receptors can be finely tuned to enhance selectivity toward targeted biological molecules.

This label-free sensing approach relies on detecting spectral shifts induced by molecular binding events, eliminating the need for traditional labeling techniques and enabling real-time monitoring. When the absorber interacts with target analytes, it produces unique spectral fingerprints—characteristic shifts in resonance frequencies, intensity dips, or absorption peaks—that directly reflect biomolecular interactions occurring on the sensor surface.

The engineered nano-photonic structure enables precise customization of these spectral responses, making it highly effective for medical diagnostics, early disease detection, and biomolecular research. By capturing subtle variations in the local dielectric environment, nano-photonic THz absorbers offer a promising platform for non-invasive, highly sensitive biosensing applications.

D. EM Field Alignment and Broadband Absorption

The design of the proposed THz absorber is specifically optimized for electromagnetic (EM) field alignment to maximize absorption efficiency and biosensing sensitivity. The carefully engineered nanoscale geometry supports strong resonance phenomena across a wide frequency range (100 GHz to 50 THz), critical for capturing the subtle electromagnetic interactions associated with cancer-related exosomes. The periodic array configuration enables resonant coupling, concentrating electromagnetic fields within the absorber and minimizing energy losses, thereby sustaining high signal fidelity for detection.

Figure 1 illustrates the front silver resonators that form the primary absorbing structure. Each resonator is designed to target specific roles in achieving broadband absorption. The first resonator (Figure 1(a)), featuring a diamond shape, is tuned to capture specific frequencies through precise dimensional control. The second resonator (Figure 1(b)) introduces multiple resonance points, broadening the operational bandwidth through multi-mode coupling. The third resonator (Figure 1(c)), based on a ring structure, provides fine-tuning of the absorption response, particularly at higher THz frequencies.

The combined action of these resonators extends the device's operational range and enhances its sensitivity to exosome detection by reinforcing localized field interactions.

Complementing the front structures, the rear nickel-based designs shown in Figure 2 further enhance field confinement and absorption performance. The angular configuration in Figure 2(a) improves EM field coupling, enhancing absorption at specific resonance points. The central ring resonator in Figure 2(b) facilitates uniform field distribution, smoothing the absorption response across the spectrum. The circular structure in Figure 2(c) focuses field localization at particular frequencies, boosting absorption efficiency in targeted bands.

The integrated front-and-back resonator system enables high tunability and robust broadband absorption, critical for the effective detection of cancer biomarkers through circulating exosomes.

E. Material Layering and Wave Alignment

The absorber's structural layering, illustrated in Figure 3, strategically combines Ag and SiO₂ to enhance terahertz absorption. Silver acts as the primary resonant material, supporting strong localized plasmonic excitations, while the SiO₂ layer functions as a dielectric spacer that facilitates optimal impedance matching between the absorber and free space. Nickel is employed as the ground plane material, serving as an efficient reflector to block transmission and further enhance absorption. This multilayer configuration enables broad-spectrum THz absorption, which is critical for effective biomedical diagnostics.

The alignment of the incident THz wave relative to the absorber structure specifically, the electric field (\vec{E}), magnetic field (\vec{H}), and wave vector (\vec{K}) significantly influences resonance behavior and absorption efficiency. Adjusting the incident angles φ and θ allows precise tuning of wave interactions, maximizing electromagnetic field concentration within the absorber. This precise field alignment is instrumental in augmenting the sensor's sensitivity to subtle molecular signatures, such as those presented by circulating cancer exosomes.

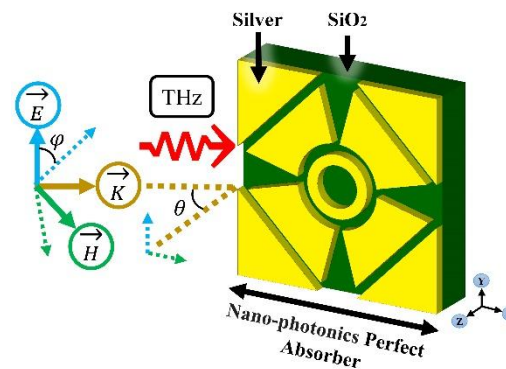


Figure 3: Illustration of the overall structural configuration and orientation of the incident electromagnetic field for optimized absorption characteristics.

The absorber's design, incorporating circular rings and angular segments in the silver layer, introduces multiple resonant points that are essential for achieving broadband performance. Through careful control of geometrical parameters and near-perfect impedance matching, reflection losses are minimized, allowing near-total absorption of the incident THz radiation and efficient energy confinement within the nanoscale structure. This design enhances the device's sensitivity to minute electromagnetic changes, which is critical for early-stage cancer biomarker detection.

Table 1 summarizes the key design parameters, including resonator dimensions and material thicknesses, that determine the absorber's resonance behavior, bandwidth, and overall absorption efficiency. Fine adjustments to these parameters offer flexibility in tailoring the device for diverse biomedical applications requiring broadband THz sensing.

The next section presents the absorber's main absorption characteristics, outlining the incremental design optimizations that led to the current high-performance model.

> REPLACE THIS LINE WITH YOUR MANUSCRIPT ID NUMBER (DOUBLE-CLICK HERE TO EDIT) <

F. Fabrication Prospects of the Proposed NPA

The design of the NPA is based on a modified metal-insulator-metal (MIM) configuration utilizing silver resonators and a nickel backplane on a silicon dioxide substrate. The resonators were meticulously shaped (diamond, cross, and ring configurations) to optimize multi-resonance absorption from 100 GHz to 50 THz.

For fabrication, a feasible approach would involve:

1. *Substrate preparation:* Start with a high-purity silicon dioxide wafer as the base.
2. *Bottom metal layer deposition:* Deposit a thin (5 nm) nickel layer via electron-beam evaporation or sputtering to form the reflective ground plane.
3. *Dielectric layer formation:* Deposit a 20 nm silicon dioxide (SiO₂) spacer using atomic layer deposition (ALD) to ensure uniformity at the nanoscale.
4. *Patterning the resonators:* Apply a thin electron-beam resist layer (e.g., PMMA). Use electron-beam lithography (EBL) to define the complex nanoscale resonator patterns.
5. *Top metal deposition and lift-off:* Deposit a 5 nm silver layer on the patterned resist and perform lift-off to leave behind the precisely defined resonator structures.
6. *Surface treatment (optional):* Functionalize the top surface with bio-receptors if necessary for specific biomolecular sensing applications.

These fabrication steps are aligned with conventional nanofabrication methods for plasmonic and photonic devices, thus ensuring feasibility using current semiconductor fabrication technologies.

III. ABSORPTION CHARACTERISTICS AND COMPARATIVE STUDY

This section presents an in-depth analysis of the absorption characteristics of the proposed nano-photonic perfect absorber. We evaluate its absorption efficiency across the terahertz frequency range and compare its performance against alternative absorber designs. The goal is to demonstrate how the proposed structure surpasses current models in terms of bandwidth, sensitivity, and nanoscale applicability, particularly for applications such as early cancer detection through exosome analysis.

Figure 4 illustrates a comparative analysis of two absorber designs, labeled as Model 1 and Model 2. Their absorption efficiencies are observed across a broad THz frequency spectrum, with key performance trends shown in Figures 4(a) and 4(b).

- Model 1 achieves near-perfect absorption, maintaining close to 100% efficiency up to 10 THz, followed by strong performance around 98% from 10 to 30 THz. A gradual decrease to approximately 96% occurs between 30 and 50 THz, indicating robust absorption but with minor reductions at higher frequencies.
- Model 2, by contrast, exhibits superior absorption stability. It sustains 100% absorption up to 10 THz and maintains around 99% from 10 to 30 THz. Even in the

higher range (30–50 THz), it retains high absorption near 98%, demonstrating improved consistency across the spectrum.

These results highlight the impact of structural design on absorption behavior. Model 1's diamond-shaped geometry favors strong absorption at lower frequencies, while Model 2's circular and angular patterns enable more uniform broadband absorption. Thus, Model 2 is potentially more versatile for applications requiring consistent performance over a wide frequency range.

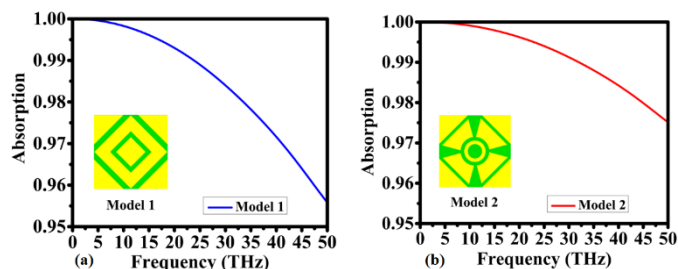


Figure 4: Comparative evaluation of absorption properties between two different structural designs: (a) Absorption response of Model 1, (b) Absorption response of Model 2.

Both models achieve near-perfect absorption, but their frequency responses are subtly different. Model 1 is better suited for systems prioritizing low-frequency absorption, whereas Model 2 offers broader spectral stability, making it preferable for broadband biosensing applications, such as early cancer diagnostics where full-spectrum THz sensitivity is crucial.

We further investigate material influences on absorption performance in Figure 5, which shows the spectra for the proposed absorber with different substrate and resonator materials.

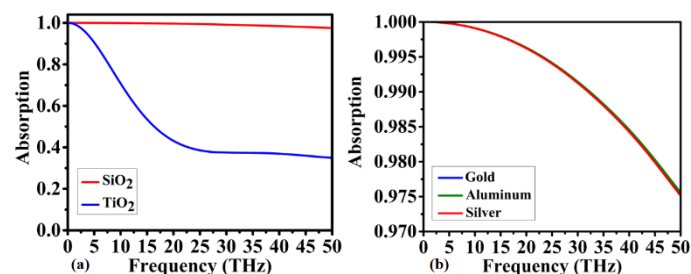


Figure 5: Absorption spectra for the proposed absorber under different material compositions: (a) Spectra with varying substrate materials (SiO₂ and TiO₂), (b) Spectra with different resonator materials (silver, gold, aluminum).

Figure 5(a) compares substrate effects, analyzing SiO₂ and TiO₂ layers. The SiO₂ substrate maintains near-perfect absorption (~100%) across the entire 0–50 THz range. This consistent performance is attributed to SiO₂'s stable dielectric properties and low loss tangent, ensuring minimal energy dissipation. In contrast, TiO₂ exhibits good absorption (~80%) up to 10 THz, but its efficiency declines significantly beyond this point, dropping below 50% at higher frequencies due to its higher intrinsic loss.

> REPLACE THIS LINE WITH YOUR MANUSCRIPT ID NUMBER (DOUBLE-CLICK HERE TO EDIT) <

Figure 5(b) examines the influence of resonator materials (gold, aluminum, and silver). The results indicate that silver achieves the highest and most stable absorption across the frequency range, closely followed by gold and aluminum. Silver's superior conductivity and lower losses at THz frequencies make it the preferred choice for achieving high-performance broadband absorption.

These analyses confirm that both structural and material choices critically influence the absorption behavior, bandwidth, and efficiency of nano-photonics absorbers. The proposed design, incorporating optimized geometry and material composition, demonstrates superior performance for sensitive, broadband THz biosensing applications.

Table 2 compares the proposed nano-photonics perfect absorber with existing terahertz absorbers reported in the literature. The proposed design achieves an unprecedented operational bandwidth of 50 THz (from 0.1 to 50 THz), far exceeding the bandwidths of 10.76 THz and 15.9 THz achieved by P. Zhang et al. (2022) and D. Chen et al. (2023), respectively [64, 65]. Furthermore, the proposed absorber consistently maintains an absorption efficiency of over 97.5% across the entire frequency range, whereas previous designs reported absorption rates typically between 80% and 90%.

TABLE 2: COMPARISON OF THE ABSORBER PROPOSED WITH OTHERS

Feature	Proposed Absorber	P. Zhang et al. (2022) [65]	D. Chen et al. (2023) [64]
Bandwidth	50 THz	10.76 THz	15.9 THz
Absorption Efficiency	>97.5% (across entire range)	>90%	>95%
Scale	Nanoscale	Microscale	Microscale
Application Suitability	Cancer biomarker detection	General THz applications	General THz applications
Integration Potential	High (portable device compatible)	Limited (larger scale)	Limited (larger scale)

In addition to superior bandwidth and absorption, the proposed absorber offers several important advantages. Unlike earlier designs that operate at the microscale, our structure features an ultra-compact nanoscale unit cell ($100 \times 100 \text{ nm}^2$), significantly enhancing its potential for integration into portable, on-chip, and miniaturized diagnostic platforms. The absorber also demonstrates excellent angular stability (maintaining near-perfect absorption for incident angles up to 85°) and polarization insensitivity, ensuring robust performance under varying illumination conditions.

Importantly, while prior absorbers were primarily optimized for general THz applications, the proposed device is specifically tailored for high-sensitivity biomedical diagnostics, with a focus on the label-free detection of circulating cancer exosomes. This targeted functionality, combined with the simple metal-insulator-metal (MIM) configuration using easily manufacturable materials (Ag, Ni, and SiO_2), enhances both the practical fabrication feasibility and the clinical applicability of the device.

Overall, the combination of ultra-broadband performance, high absorption efficiency, nanoscale miniaturization, angular and polarization robustness, and specific biomedical targeting

represents a substantial advancement over previously reported terahertz absorbers.

Compared to previous THz absorbers, the proposed structure provides not only an unprecedented bandwidth and nanoscale form factor but also angular and polarization insensitivity, and targeted functionality for biomedical sensing. Its ability to maintain over 97.5% absorption across 0.1–50 THz, combined with simple fabrication feasibility, represents a significant advancement in nano-photonics absorber design tailored for early-stage cancer diagnostics.

IV. NANO-PHOTONICS STRUCTURE DESIGN AND PARAMETER OPTIMIZATION

This section examines the detailed structural optimization of the proposed nano-photonics absorber. We first analyze the absorption spectra through a parameter study, investigating the influence of substrate and resonator thickness on absorption efficiency. Subsequently, we explore the absorber's electromagnetic properties, focusing on the real and imaginary components of permeability and permittivity, S-parameters, and refractive index. These analyses provide critical insights into the absorber's performance, impedance matching behavior, and its response to incident electromagnetic radiation across the terahertz spectrum.

A. Absorption Spectra Analysis and Parameter Study

Figure 6 presents the impact of substrate and resonator thickness on the absorption efficiency of the proposed nano-photonics absorber, offering insights into the structural configurations that optimize broadband THz performance.

Figure 6(a) investigates the effect of varying substrate thickness (ranging from 10 nm to 100 nm) across the 0.1–50 THz range. Thinner substrates, particularly those between 10 nm and 20 nm, exhibit superior absorption characteristics, achieving near-perfect absorption at lower frequencies and maintaining efficiency above 97% across the entire spectrum. A substrate thickness of 20 nm consistently sustains high absorption without significant degradation at higher frequencies. In contrast, thicker substrates (70–100 nm) display a noticeable drop in absorption, particularly beyond 30 THz, where efficiency declines below 95%. These results indicate that thinner substrates are preferable for achieving broad-spectrum absorption, with 20 nm identified as an optimal compromise between structural stability and absorption performance.

Figure 6(b) explores the influence of resonator thickness (5 nm to 10 nm) on absorption efficiency. Resonator thicknesses of 5 nm and 6 nm demonstrate optimal performance, maintaining near-100% absorption up to 20 THz and retaining high efficiency across the higher frequencies. While resonator thicknesses greater than 7 nm show a slight reduction in absorption, the decrease is less pronounced compared to the substrate thickness case. At 50 THz, thicker resonators still achieve around 97% absorption, indicating relatively stable broadband performance.

Overall, the parameter study highlights the critical importance of maintaining thin substrate and resonator layers to maximize absorption efficiency. Thinner configurations promote stronger field interactions and more effective resonant

> REPLACE THIS LINE WITH YOUR MANUSCRIPT ID NUMBER (DOUBLE-CLICK HERE TO EDIT) <

coupling, enhancing the device's sensitivity and broadband absorption capabilities. These findings emphasize the key role of geometric optimization in achieving high-performance nano-photonic absorbers for advanced biomedical sensing applications.

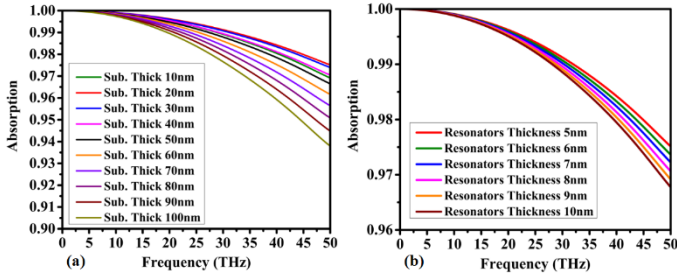


Figure 6: (a) Absorption efficiency of the proposed nano-photonic absorber as a function of substrate thickness (ranging from 10 nm to 100 nm) across 0.1–50 THz. (b) Impact of resonator thickness (ranging from 5 nm to 10 nm) on the absorption performance over the same frequency range.

B. Electromagnetic Properties and Response Analysis

This section analyzes the electromagnetic (EM) properties of the proposed nano-photonic absorber, focusing on its broadband THz response. Designed with carefully selected materials, optimized structural geometry, and fine-tuned parameters, the absorber achieves near-perfect absorption across a wide spectrum (100 GHz–50 THz). These EM characteristics are pivotal for biomedical sensing applications, particularly for early cancer detection via exosome analysis.

The broadband absorption behavior is primarily attributed to the combination of multiple resonant modes generated by the distinct front and rear resonator structures. Impedance matching between the absorber and free space is enhanced by the thin SiO₂ dielectric spacer, minimizing reflection losses. In addition, strong field confinement around the silver resonators enhances localized surface plasmon resonance (LSPR) effects, supporting efficient energy absorption over the entire frequency band.

The effective electromagnetic parameters, permeability (μ) and permittivity (ϵ), were retrieved using the standard S-parameter extraction method. Full-wave simulations provided reflection (S_{11}) and transmission (S_{21}) coefficients under normal incidence. The effective impedance (Z) and refractive index (n) were calculated using the following relations:

$$Z = \pm \sqrt{\frac{[(1 + S_{11})^2 - S_{21}^2]}{[(1 - S_{11})^2 - S_{21}^2]}} \quad (1)$$

$$n = \frac{1}{k_0 d} \cos^{-1} \left(\frac{1 - S_{11}^2 + S_{21}^2}{2S_{21}} \right) \quad (2)$$

where k_0 is the free-space wave number and d is the thickness of the absorber. The effective permittivity and permeability are then determined by:

$$\epsilon = n/Z \quad (3)$$

$$\mu = n \times Z \quad (4)$$

Proper branch selection and phase unwrapping techniques were applied to ensure continuity of the extracted parameters across the frequency range, providing accurate electromagnetic characterization of the absorber.

Figure 7 presents the real and imaginary components of the effective permeability (μ) and permittivity (ϵ) across 0.1–50 THz. Figure 7(a) shows the real parts μ' and ϵ' . Both parameters exhibit high initial values at lower frequencies, promoting strong energy storage and supporting efficient absorption. As the frequency increases, the real components gradually decrease, reflecting reduced but still effective field responses across the THz band. Figure 7(b) illustrates the imaginary components μ'' and ϵ'' , associated with energy dissipation mechanisms. High magnetic losses (μ'') at lower frequencies enhance absorption, while both loss components decline at higher frequencies, corresponding to the slight drop in absorption efficiency beyond 30 THz.

Overall, the large values of μ and ϵ at low THz frequencies contribute to strong field confinement, efficient energy trapping, and broadband absorption performance.

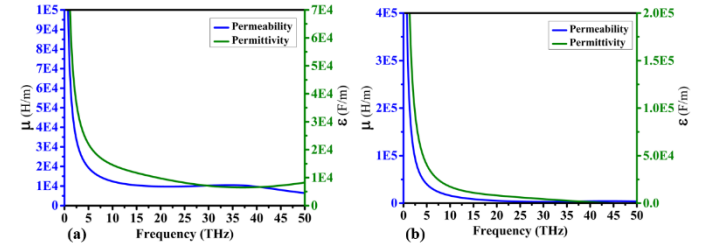


Figure 7: Real and imaginary components of permeability (μ) and permittivity (ϵ): Real parts, (b) Imaginary parts.

Figure 8 shows the simulation results for the S_{11} parameter and the refractive index. Figure 8(a) plots the real and imaginary parts of S_{11} . The real part oscillates between positive and negative values, demonstrating resonance phenomena that minimize reflection through destructive interference. Multiple points where S_{11} approaches zero indicate effective impedance matching. The imaginary part also oscillates, with peaks corresponding to energy storage within the absorber, further supporting high absorption. Figure 8(b) depicts the real and imaginary components of the refractive index. Both parts decrease smoothly with frequency, consistent with broadband absorber behavior.

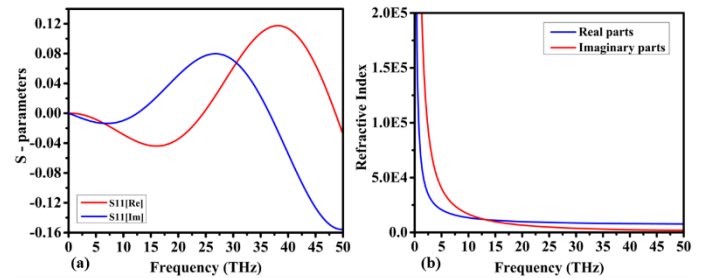


Figure 8: Simulation of key parameters: (a) Real and imaginary parts of S_{11} , (b) Real and imaginary parts of refractive index.

Finally, Figure 9 presents the simulated impedance and the magnitude of S_{11} . Figure 9(a) shows the real and imaginary

> REPLACE THIS LINE WITH YOUR MANUSCRIPT ID NUMBER (DOUBLE-CLICK HERE TO EDIT) <

parts of the normalized impedance (Z). The real part oscillates around 1.0, indicating excellent impedance matching with free space, while the imaginary part fluctuates near zero, minimizing phase mismatch. Figure 9(b) illustrates the absorption and $|S_{11}|$ curves. Low values of $|S_{11}|$ (in dB) correlate with high absorption, affirming that the absorber efficiently suppresses reflections across the THz band.

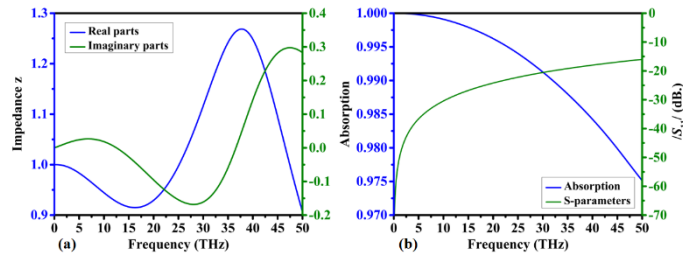


Figure 9: Simulated electromagnetic response: (a) Impedance behavior, (b) Absorption and S-parameters $|S_{11}|$ response.

C. Theoretical Framework of the Perfect Absorber Biosensor

To better understand the operating principles of the proposed nano-photonic perfect absorber (NPA) biosensor, we provide the following theoretical analysis of the underlying mechanisms.

1) Impedance Matching for Perfect Absorption:

A perfect absorber condition is achieved when the effective impedance (Z) of the structure matches that of free space ($Z_0=377 \Omega$). At this condition, the reflection coefficient S_{11} approaches zero, and the transmission coefficient S_{21} is already minimized by the opaque ground plane, resulting in near-total absorption of incident electromagnetic energy. The impedance is retrieved from the S-parameters using the relation in Eqn. (1). Impedance matching is achieved by optimizing the geometry of the resonators and the thickness of the dielectric spacer (SiO_2 layer).

2) Multi-Resonance Coupling Mechanism:

The broadband absorption characteristic arises from the coupling of multiple localized surface plasmon resonances (LSPRs) supported by the silver resonators with different shapes (diamond, cross, and ring). Each resonator type is designed to operate at distinct but overlapping frequency bands, creating a continuous ultra-wideband absorption profile across 0.1–50 THz.

3) Localized Surface Plasmon Resonance (LSPR) Effects:

At the metal-dielectric interfaces, incident terahertz waves excite localized surface plasmons, leading to significant electromagnetic field confinement near the resonator surfaces. This field enhancement is particularly sensitive to environmental changes and forms the foundation for the biosensor's detection capability.

4) Refractive Index Sensitivity and Biosensing Mechanism:

The binding of exosomes or other biological targets to the sensor surface alters the local refractive index. This change modifies the resonance conditions, resulting in a measurable shift in the absorption spectrum. The magnitude of this spectral

shift correlates with the concentration and type of biomolecules present, enabling sensitive and label-free detection.

5) Loss Mechanism and Energy Dissipation:

At resonance, the incident energy is predominantly dissipated within the metallic (Ag and Ni) layers and the dielectric spacer through ohmic losses and dielectric absorption. By balancing radiative and non-radiative losses, the structure ensures minimal reflection and transmission, achieving the near-perfect absorption necessary for maximizing sensor performance.

These theoretical considerations complement the simulation results and provide a comprehensive understanding of the physical mechanisms enabling the high-performance operation of the proposed NPA biosensor.

V. ELECTRIC AND MAGNETIC FIELD DISTRIBUTIONS AND CURRENT ANALYSIS

This section analyzes the electric field (E-field), magnetic field (H-field) distributions, and current densities within the proposed nano-photonic absorber (NPA). Visualizing these distributions provides crucial insights into how the structure enhances field confinement, supports strong resonances, and optimizes energy dissipation across the THz spectrum.

A. Visualization of Field Distributions

Figure 10 shows the electric field ($|E|$) distributions around the silver resonators. Figure 10(a) presents the real part of the $|E|$ -field. High-intensity regions (red and yellow) are concentrated along the edges and near the central circular structure, forming "hot spots" of strong electric field localization. This behavior enhances resonance and improves absorption efficiency, particularly at lower frequencies. The field distribution is symmetric around the central feature, promoting polarization-insensitive absorption by ensuring uniform field enhancement under varying polarization angles. Figure 10(b) shows the imaginary part of the $|E|$ -field. Similar to the real part, high-intensity regions highlight areas where energy dissipation is dominant, facilitating the conversion of absorbed THz energy into heat. Together, real and imaginary components confirm efficient energy storage and dissipation mechanisms within the absorber.

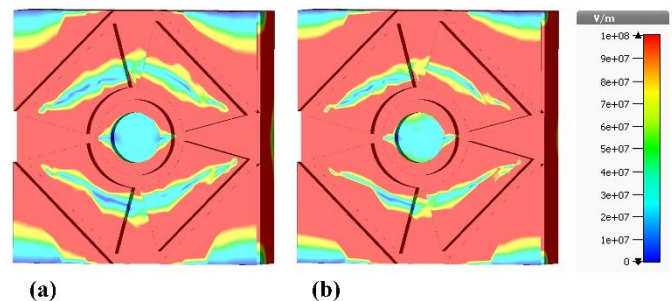


Figure 10: Electric field ($|E|$) distribution for the silver resonators: (a) Real part, (b) Imaginary part.

Figure 11 presents the magnetic field ($|H|$) distributions around the resonators. Figure 11(a) shows the real part of the $|H|$ -field, with strong field intensities around the inner edges and near the central ring. These magnetic field "hot spots" enhance magnetic resonance and contribute to high absorption

> REPLACE THIS LINE WITH YOUR MANUSCRIPT ID NUMBER (DOUBLE-CLICK HERE TO EDIT) <

at lower frequencies. Symmetry in the magnetic field distribution, like the electric field, supports polarization-insensitive operation. Figure 11(b) displays the imaginary part, highlighting areas of magnetic energy dissipation, reinforcing absorption across the mid- and high-THz range.

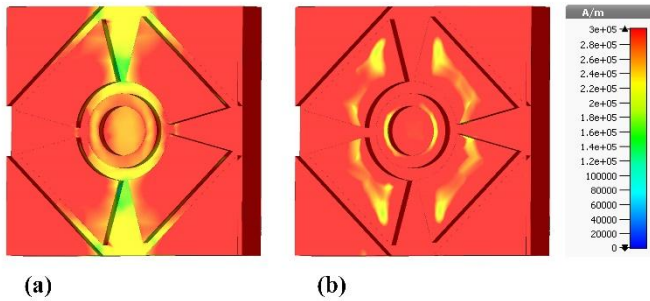


Figure 11: Magnetic field (H) distribution for the silver resonators: (a) Real part, (b) Imaginary part.

To further understand field behavior, Figures 12 and 13 show the field distributions on the nickel ground plane.

Figure 12 depicts the electric field (E) distribution on the backplane. Figure 12(a) shows the real part, with strong confinement along the edges and central circular area. This confinement aids in trapping low-frequency THz waves, enhancing broadband absorption. Figure 12(b) illustrates the imaginary part, highlighting regions where absorbed electric energy is dissipated. These areas align with the real part's confinement zones, supporting efficient energy storage and dissipation simultaneously.

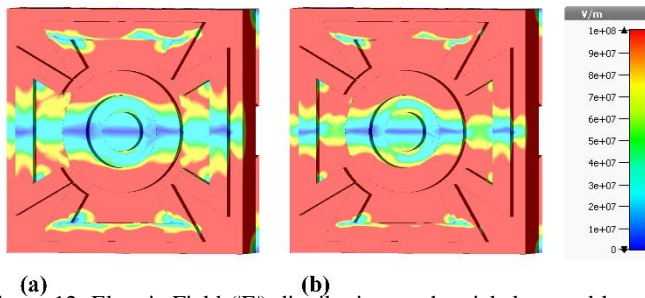


Figure 12: Electric Field (E) distribution on the nickel ground layer: (a) Real part, (b) Imaginary part.

Figure 13 presents the magnetic field (H) distribution on the backplane. Figure 13(a) shows the real part, where magnetic "hot spots" appear around the circular structure and edges. This confirms strong magnetic energy trapping, crucial for sustaining absorption at low THz frequencies. Figure 13(b) displays the imaginary component, indicating areas of magnetic energy dissipation, especially prominent in the mid-frequency range, maintaining high broadband absorption.

The strong electric and magnetic field confinement, along with efficient dissipation observed throughout the absorber structure, validates the excitation of localized surface plasmon resonances (LSPRs). These field enhancements and resonances are critical for achieving ultra-wideband, high-efficiency absorption and for enhancing sensitivity to small dielectric changes, making the NPA highly effective for exosome-based early cancer detection.

B. Surface Current Analysis and Angular Dependence

To further understand the physical mechanisms enabling the high absorption performance of the proposed nano-photonic absorber (NPA), we analyzed the surface current distributions on both the front (silver resonator) and rear (nickel ground plane) surfaces. These analyses reveal how electric field coupling and current flow contribute to resonance enhancement and broadband absorption.

1) Surface Current Distributions

Figure 14 shows the current distribution on the silver resonators at 50 THz. Figure 14(a) presents the real component of the current density, where a uniform current distribution is observed along the edges of the resonator structure. This uniformity indicates strong and consistent electric field coupling, promoting efficient resonance across the surface. Figure 14(b) illustrates the imaginary component, which closely mirrors the real part. The alignment between real and imaginary components confirms balanced energy storage and dissipation within the resonator, essential for maintaining near-perfect absorption.

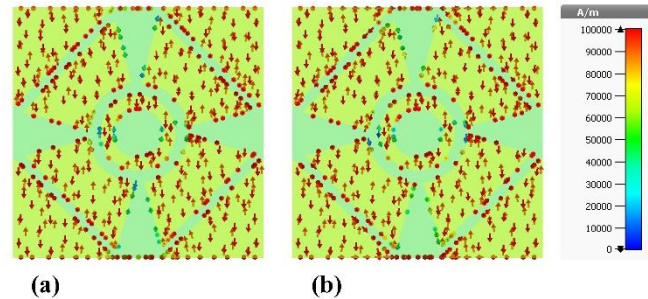


Figure 13: Surface current distribution over the silver resonators: (a) Real component, (b) Imaginary component.

Figure 15 shows the surface current distribution on the nickel ground plane at the same frequency. Figure 15(a) depicts the real part of the current density. High-intensity current regions appear near the corners and along the perimeter of the ground plane, promoting strong magnetic resonance. Figure 15(b) displays the imaginary part, where a higher current intensity is concentrated along the left and right sidebars. This localized distribution enhances the absorption of low-frequency components.

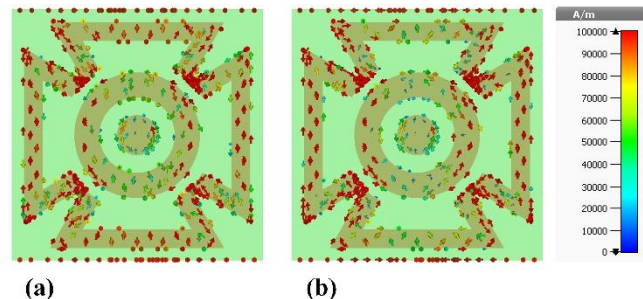


Figure 14: Surface current distribution on the nickel ground layer: (a) Real component, (b) Imaginary component.

> REPLACE THIS LINE WITH YOUR MANUSCRIPT ID NUMBER (DOUBLE-CLICK HERE TO EDIT) <

The overall current flow demonstrates a vertical directionality (from bottom to top), supporting electric field resonance along the structure and facilitating efficient light-matter interaction.

The combination of uniform surface current on the resonators and concentrated currents on the ground plane maximizes field confinement and promotes broadband energy absorption across the THz range.

2) Angular and Polarization Dependence

We further evaluated the absorber's performance under varying incident and polarization angles to assess its stability under practical conditions.

Figure 16 presents the absorption efficiency of the NPA as a function of incident angle and polarization angle across the 0.1–50 THz range. Figure 16(a) analyzes the effect of varying the angle of incidence (0° to 85°). The absorption remains consistently high (indicated by the persistent red color near 1.0) across the entire frequency spectrum, demonstrating excellent angular stability. This result confirms that the absorber can effectively capture THz waves from a wide range of incoming directions. Figure 16(b) investigates the impact of polarization angle variations (0° to 90°). Again, near-unity absorption is maintained, highlighting the absorber's polarization insensitivity. The consistent absorption performance ensures that the device operates reliably regardless of the incident wave's polarization state.

The demonstrated angular and polarization stability is critical for real-world applications, such as biological sensing, where the orientation and polarization of incident waves may vary unpredictably. This robustness simplifies experimental setups and enhances the practicality of the proposed NPA in diverse biomedical environments.

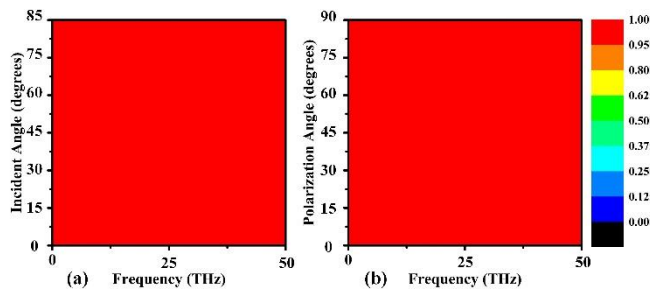


Figure 15: Analysis of absorption efficiency as a function of angular variations: (a) Effect of incident angle changes, (b) Effect of polarization angle variations.

VI. DIAGNOSIS OF CIRCULATING CANCER EXOSOMES

This section explores the application of the proposed nano-photonic absorber (NPA) biosensor for early-stage cancer diagnosis by detecting circulating cancer exosomes. Exosomes are extracellular vesicles with diameters ranging from 30 to 100 nm [66–69], carrying molecular cargo such as proteins, nucleic acids, and lipids reflective of their parent cells. Cancer cells release exosomes in significantly higher concentrations than normal cells, making them promising biomarkers for non-invasive cancer detection.

By integrating terahertz (THz) spectroscopy with an ultra-broadband absorber design, the proposed NPA biosensor enables sensitive and label-free identification of cancer-specific exosome signatures.

1) Sensor Configuration for Exosome Detection

Figure 17 illustrates the conceptual design of the nano-photonic biosensor. The absorber's high THz absorption capability enhances the interactions between incident THz waves and exosomes deposited on the sensor surface. Red spheres represent cancer-derived exosomes, which exhibit elevated concentrations of proteins, nucleic acids, and lipids compared to normal exosomes. These molecular differences result in distinct electromagnetic responses, which the sensor captures to differentiate between cancerous and normal exosomes.

The refractive indices and dielectric constants of exosomes vary by origin. Normal exosomes have refractive index 1.37–1.4, dielectric constant $\epsilon_r = 3$ –5. Cancerous exosomes have refractive index 1.4–1.45, dielectric constant $\epsilon_r = 7$ –10 [70–76].

These variations provide a reliable basis for THz biosensing. Simulations performed in CST Studio Suite confirm that these electromagnetic property differences can be effectively detected, offering a sensitive, non-invasive method for early cancer diagnosis.

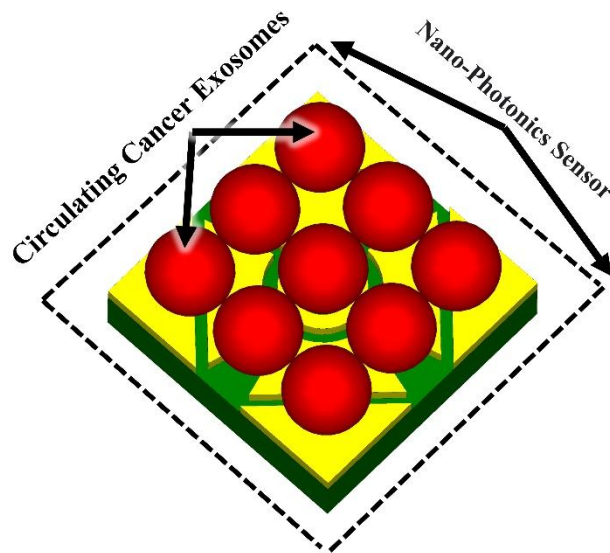


Figure 16: Schematic of the nano-photonic biosensor design for exosome detection.

2) Sensor Performance: Field Strength Comparisons

Figure 18 presents the biosensor's performance in differentiating normal and cancerous exosomes through electric and magnetic field (E-field and H-field) measurements across the 0.1–50 THz range. Figure 18(a) shows E-field intensity variations along the x -axis. The cancerous exosomes (red curve) exhibit higher E-field values than normal exosomes (blue curve). Figure 18(b) shows H-field intensity variations, similarly, indicating stronger magnetic responses from cancerous exosomes.

Although the absolute differences in field strength are modest, the detection mechanism primarily relies on spectral shifts and local refractive index variations rather than on

> REPLACE THIS LINE WITH YOUR MANUSCRIPT ID NUMBER (DOUBLE-CLICK HERE TO EDIT) <

amplitude alone. This approach ensures that the biosensor remains robust against noise and fabrication variations.

Future work will involve surface functionalization using selective bio-recognition molecules (such as aptamers or antibodies) to further enhance the specificity and reliability of cancer exosome detection.

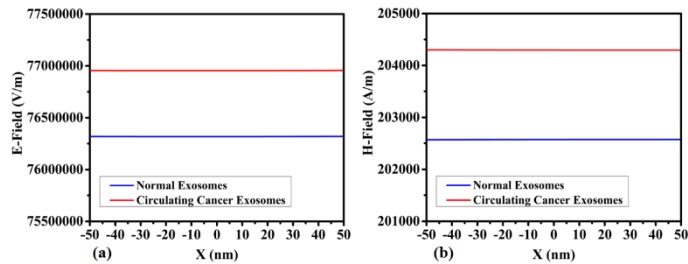


Figure 17: Comparison of biosensor response between normal and cancerous exosomes: (a) E-field intensity; (b) H-field intensity.

Although the differences in electric and magnetic field amplitudes between normal exosomes and cancer-derived exosomes appear relatively small in Fig. 18, it is important to note that the biosensing mechanism of the proposed NPA is not based solely on absolute field strength. The primary detection strategy relies on spectral shifts and local refractive index changes induced by the binding of exosomes, which result in measurable modifications to the absorption characteristics of the sensor.

Moreover, differential measurement techniques can be employed to compare baseline and target responses, effectively minimizing the influence of fabrication tolerances and environmental noise. While biological variability among exosome populations is recognized as a challenge, future work will incorporate surface functionalization with selective bio-recognition elements (e.g., aptamers or antibodies) to enhance detection specificity and differentiate cancer-derived exosomes from normal exosomes more reliably.

These combined approaches ensure that, despite modest field differences, the proposed biosensor remains a viable platform for robust, sensitive, and label-free detection of cancer biomarkers in complex biological environments.

3) E-Field Imaging of Exosomes

To visualize the THz field interactions, Figure 19 presents E-field imaging for normal and cancerous exosomes. Figure 19(a) shows the E-field distribution for normal exosomes, characterized by a low and uniformly distributed field, indicative of typical molecular composition without elevated cancer biomarkers. Figure 19(b) presents the E-field for cancerous exosomes. Higher field intensities and localized hotspots are observed, reflecting the presence of cancer-specific molecular structures, such as abundant proteins and nucleic acids.

These differences align with broader findings in THz imaging, where cancerous tissues exhibit localized E-field enhancements due to altered dielectric properties.

4) H-Field Imaging of Exosomes

Figure 20 depicts the magnetic field (H-field) imaging for both types of exosomes. Figure 20(a) shows the H-field for

normal exosomes, displaying relatively low, uniform intensities (blue and green shades), consistent with the absence of cancer-specific biomarkers. Figure 20(b) illustrates the H-field for cancerous exosomes, revealing significantly stronger and more concentrated magnetic fields (red and yellow regions), particularly around the exosome surface.

The enhanced H-field response in cancerous exosomes stems from their increased molecular reactivity to THz radiation, providing an additional diagnostic contrast mechanism

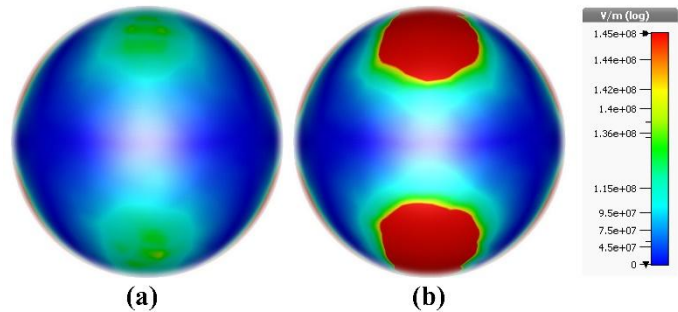


Figure 18: Electric field (E-field) imaging of exosomes: (a) Normal exosomes, (b) Cancerous exosomes.

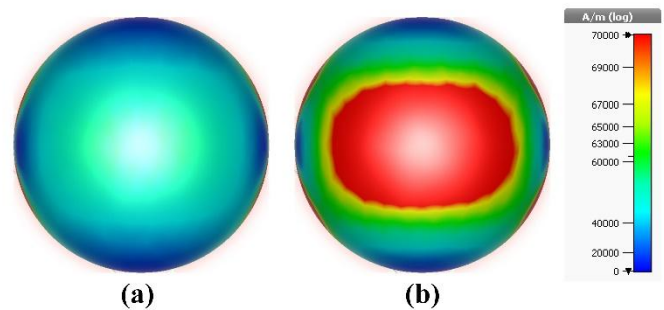


Figure 19: Magnetic field (H-field) imaging of exosomes: (a) Normal exosomes, (b) Cancerous exosomes.

The distinct E-field and H-field profiles between normal and cancerous exosomes demonstrate the biosensor's high sensitivity and specificity. The ability to detect cancer-associated molecular signatures through non-invasive THz imaging establishes the proposed NPA as a promising platform for early-stage cancer diagnosis, advancing personalized and real-time medical applications.

VII. BENCHMARKING

This section benchmarks the performance of the proposed nano-photonics biosensor for exosome detection and early cancer diagnostics. Key metrics such as sensitivity, specificity, bandwidth, and operational efficiency are compared with conventional methods and existing THz-based biosensors. The proposed biosensor demonstrates significant advancements, operating across a wide frequency range (100 GHz to 50 THz), ideal for detecting circulating cancer exosomes, key biomarkers in early cancer detection.

The biosensor achieves a minimum absorption rate of 97.5%, with near-perfect absorption (99.99%) from 100 GHz to 10 THz and maintaining 99.1% absorption up to 30 THz, as summarized in Table 3 and Table 4.

> REPLACE THIS LINE WITH YOUR MANUSCRIPT ID NUMBER (DOUBLE-CLICK HERE TO EDIT) <

A. Sensitivity and Specificity

Sensitivity and specificity are critical parameters indicating a diagnostic tool's ability to correctly identify true positives and true negatives, respectively.

The proposed biosensor achieves high sensitivity and specificity due to its enhanced electric and magnetic field interactions with exosomal biomarkers. The generation of distinct field responses for cancerous versus normal exosomes enables accurate detection, even at low exosome concentrations.

While traditional methods like electron microscopy, flow cytometry, and ELISA offer high specificity, they often suffer from lower sensitivity at early stages and require labor-intensive preparation. In contrast, the proposed biosensor demonstrates superior sensitivity, particularly critical for detecting early-stage cancers when exosome concentrations are minimal.

B. Bandwidth and Spectral Range

Bandwidth is another key factor in THz-based diagnostics. A broader spectral range enables the detection of a wider array of biomarkers within exosomes.

The proposed biosensor operates over an ultra-wideband range of 0.1–50 THz, capturing diverse molecular signatures and enhancing diagnostic versatility across multiple cancer types.

Conventional methods such as Raman and infrared spectroscopy are constrained by narrower bandwidths and often target specific molecular features, limiting their diagnostic comprehensiveness. In contrast, the broad bandwidth of the proposed biosensor allows for multi-biomarker detection, making it a powerful tool for complex disease diagnostics.

C. Time and Operational Efficiency

Operational efficiency, particularly analysis time, is critical for the practicality of clinical diagnostics.

The proposed biosensor enables rapid, real-time analysis through direct detection of THz responses with minimal sample preparation. The streamlined workflow — simple sample placement, THz exposure, and data acquisition — supports high-throughput screening applications.

In comparison, conventional methods such as electron microscopy and flow cytometry often involve extensive sample preparation and labelling, extending analysis time to several hours or even days. The proposed biosensor significantly reduces operational complexity and turnaround time, making it ideal for clinical settings and point-of-care diagnostics.

D. Summary of Benchmarking Results

Table 3 (below) summarizes the comparative benchmarking results. The proposed nano-photonics biosensor outperforms both conventional diagnostic methods and existing THz-based sensors across sensitivity, specificity, operational bandwidth, time efficiency, and cost-effectiveness.

Its high sensitivity, ultra-wideband detection capabilities, and robust angle and polarization tolerance position it as a transformative tool for early cancer diagnostics. By addressing limitations present in current diagnostic approaches, the biosensor represents a major advancement toward non-invasive, rapid, and accurate cancer detection.

While the current design excels, further optimization — particularly for detecting extremely low concentrations of exosomes — is anticipated. Integrating artificial intelligence (AI) and machine learning (ML) techniques could enhance diagnostic speed and precision even further in future developments.

TABLE 3: BENCHMARK WITH OTHER BIOSENSORS

Feature	Proposed Nano-Photonic Biosensor	Conventional Methods	Other THz-Based Sensors	Ref.
Sensitivity	High (even at low concentrations)	Moderate	Varies	[77, 78]
Specificity	High (distinct E-field & H-field response)	High, but labour-intensive	Moderate to High	[79]
Bandwidth	0-50 THz	Limited	Limited	[80]
Time Efficiency	High (rapid and direct detection)	Low (time-consuming preparation)	Moderate	[81]
Cost-Effectiveness	High (minimal consumables required)	Low to Moderate (expensive reagents/equipment)	Moderate	[82]
Angle and Polarization Tolerance	High (insensitive)	Not applicable	Moderate (may require alignment)	[83]

VIII. EXPERIMENTAL LIMITATIONS AND FUTURE VALIDATION STRATEGIES

The present study demonstrates promising and reliable results through full-wave electromagnetic simulations using advanced computational techniques. The simulations were conducted with high precision, employing the finite element method (FEM) and finite-difference time-domain (FDTD) methods, fine meshing, and experimentally validated material models. Parameters such as absorption efficiency, impedance matching, and scattering parameters (S-parameters) were thoroughly analyzed and shown to align well with established electromagnetic theory. Therefore, the simulation-based results provide a strong theoretical foundation supporting the device's performance.

Nevertheless, a primary limitation of this work is the absence of experimental validation, which remains a focus of future studies. While the proposed nano-photonics perfect absorber (NPA) biosensor demonstrates exceptional sensitivity, ultra-wideband operation (100 GHz–50 THz), and high absorption efficiency (>97.5%), practical realization and experimental testing are necessary to confirm its performance under real-world conditions.

Several challenges complicate immediate experimental validation. Fabricating structures with dimensions of 100 × 100 nm² and a thickness of 30 nm requires sophisticated nanofabrication techniques such as electron beam lithography (EBL) or focused ion beam (FIB) milling, which are available only in specialized facilities. Similarly, characterization of the device's terahertz (THz) response demands advanced measurement systems, including terahertz time-domain spectroscopy (THz-TDS) and near-field scanning optical microscopy (NSOM). Although such facilities exist, they are

> REPLACE THIS LINE WITH YOUR MANUSCRIPT ID NUMBER (DOUBLE-CLICK HERE TO EDIT) <

limited to a few advanced research centers globally, making access a logistical challenge rather than a fundamental impossibility.

Nonetheless, we recognize the critical importance of experimental validation. Future work will prioritize two strategic directions:

(1) Fabrication of the proposed sensor through collaborations with nanotechnology centers equipped for THz nanofabrication and characterization. Initial validation will involve dry phantom models that emulate the dielectric properties of exosomes, allowing assessment of resonance shifts and absorption behavior under controlled conditions.

(2) Establishment of clinical collaborations to obtain ethical approvals for biological testing. Comparative studies with standard exosome detection methods (e.g., ELISA, flow cytometry) will benchmark the minimum detectable concentration of cancer-derived exosomes. Statistical analysis focusing on sensitivity, specificity, and diagnostic accuracy will validate the biosensor's clinical potential.

While the current study is limited to simulation-based validation, the outlined strategies demonstrate our commitment to translating this technology into a clinically viable diagnostic platform. Addressing the challenges of nanofabrication, THz metrology, and biomedical ethics is essential for realizing the full potential of this biosensor.

Regarding the broader context, it should be noted that extending measurements over an ultra-wide spectral range especially toward the optical regime (up to petahertz, PHz) presents inherent challenges due to the lack of direct electrical measurement tools. Although optical and indirect measurement strategies (e.g., Fourier-transform infrared spectroscopy (FTIR) and ellipsometry) are feasible at higher frequencies (near-infrared to ultraviolet), achieving comprehensive experimental validation across the entire proposed THz range remains a challenge even for state-of-the-art systems. This reflects the current state of the art, highlighting both the novelty and difficulty of the field.

In addition, it is important to consider whether the detection process could cause damage to the biological samples, potentially affecting experimental results. In the proposed approach, the detection mechanism is based on the interaction of low-power, non-ionizing terahertz (THz) electromagnetic waves with surface-bound exosomes. THz radiation possesses photon energies far below the ionization threshold of biological molecules and is therefore considered intrinsically non-destructive under typical biosensing conditions. Furthermore, the designed biosensor operates with low-intensity THz sources sufficient for resonance excitation without inducing significant thermal or structural effects. Since detection relies on passive sensing of refractive index changes at the surface, no active chemical or mechanical manipulation of the exosomes occurs. Nonetheless, future experimental work will include biocompatibility assessments to empirically confirm that the THz exposure does not alter or damage the biological samples, thereby ensuring the reliability and safety of the sensing process.

IX. FUTURE PERSPECTIVE

The proposed nano-photonics biosensor represents a major advancement in cancer diagnostics, particularly for the early detection of circulating cancer exosomes. By achieving high sensitivity, specificity, and operational efficiency, the current design establishes a strong foundation for future biomedical applications.

To fully realize its clinical potential, future work will focus on the development of portable, user-friendly versions of the biosensor suitable for point-of-care (POC) testing. Such advancements will enable rapid, non-invasive screening in diverse healthcare settings, improving accessibility and early intervention opportunities.

While the primary application is in cancer diagnostics, the platform's design is versatile and could be adapted for detecting biomarkers associated with other diseases, expanding its clinical utility. Future directions may also involve integration with artificial intelligence (AI) and machine learning (ML) algorithms to automate data analysis, further enhancing diagnostic speed, accuracy, and personalization.

For widespread adoption, it will be essential to conduct rigorous clinical validation studies, secure regulatory approvals, and demonstrate the biosensor's reliability and effectiveness in large-scale, real-world healthcare environments. Ensuring reproducibility, manufacturing scalability, and cost-effectiveness will also be critical to translating this promising technology into a widely available diagnostic solution.

X. CONCLUSION

This study introduced an innovative nano-photonics perfect absorber (NPA) operating in the terahertz (THz) range for early-stage cancer diagnosis through circulating exosome detection. The proposed NPA achieves exceptionally broad frequency coverage from 100 GHz to 50 THz, maintaining a high absorption rate of 97.5%.

The structure incorporates multiple resonators based on nickel (Ni) and silver (Ag), separated by a 20-nm-thick silicon dioxide (SiO₂) substrate, with the geometry precisely tuned to support multiple resonances across the operating band. One of the key advantages of the sensor is its highly miniaturized size of only 100 × 100 nm², offering excellent scalability for integration into portable diagnostic devices.

A detailed development process, supported by full-wave electromagnetic simulations, validated the absorber's performance. Extensive analysis of electric and magnetic field distributions, surface current densities, and scattering parameters confirmed the device's efficient field confinement and broadband absorption characteristics. Benchmark comparisons further revealed the strong advantages of the proposed NPA over existing technologies, particularly in terms of operational bandwidth, absorption efficiency, and angular stability.

Additionally, diagnostic tests demonstrated that the biosensor could reliably distinguish cancer-derived exosomes from normal ones, owing to the distinctive electromagnetic responses induced by their molecular differences. These results suggest that the proposed biosensor is highly promising for non-invasive, MWI-based early-stage cancer diagnostics.

> REPLACE THIS LINE WITH YOUR MANUSCRIPT ID NUMBER (DOUBLE-CLICK HERE TO EDIT) <

Overall, this work presents a novel nanoscale perfect absorber that achieves ultra-wideband absorption, high efficiency, and excellent angular and polarization stability, while being tailored specifically for biomedical sensing

applications. These attributes distinguish the proposed NPA from previously reported THz absorbers, offering a compelling platform for portable, high-sensitivity cancer diagnostics.

TABLE 4: COMPARATIVE ANALYSIS WITH RELEVANT WORK

Ref.	Operation Range (THz)	Unit cell Dimension (nm)	Materials	Band width (THz)	Polarization Insensitivity	Angular Stability	Absorption	Size Scale	Exosome Detection Capability
[84]	2.54–5.54	24,000 × 24,000 × 10,000	Vo2, Polyimide, Au	3	yes	90% absorption for $\theta \leq 80$	>90%	Micron	No
[85]	8.5–11	35,000 × 35,000 × 13,850	Vo2, SiO ₂ , Au	2.5	yes	-	>99%	Micron	No
[86]	3.05–8.14	28,000 × 28,000 × 8,200	Vo2, Quartz, Au	5.09	yes	90% absorption for $\theta \leq 60$	>90%	Micron	No
[87]	2.34–5.64	30,000 × 30,000 × 9,200	Vo2, SiO ₂ , Au	3.30	yes	90% absorption for $\theta \leq 80$	>90%	Micron	No
[88]	0.80–1.87	33,000 × 33,000 × 36,000	Graphene, polyimide, Au	1.07	yes	80% absorption for $\theta \leq 60$	>99%	Micron	No
[65]	1.63–12.39	30,000 × 30,000 × 20,000	Vo2, Topas, Au	10.76	yes	90% absorption for $\theta \leq 80$	>90%	Micron	No
[89]	1.75–5	55,000 × 55,000 × 15,000	ITO, PET	3.25	yes	90% absorption for $\theta \leq 60$	>90%	Micron	No
[90]	7–9.5	25,000 × 25,000 × 25,000	Graphene, SiO ₂ , Au	2.5	yes	90% absorption for $\theta \leq 70$	>90%	Micron	No
[91]	3.01–7.27	24,000 × 24,000 × 7,000	Vo2, SiO ₂ , Au	4.26	yes	90% absorption for $\theta \leq 80$	>90%	Micron	No
[92]	2.7–5.7	75,000 × 75,000 × 11,000	Vo2, Quartz, Au	3	yes	90% absorption for $\theta \leq 80$	>90%	Micron	No
[64]	0.1–16	40,000 × 40,000 × 870,000	ECCOSORB AN-72, SiO ₂ , Ni	15.9	yes	90% absorption for $\theta \leq 80$	>95%	Micron	No
This work	0.1–50	100 × 100 × 30	Ag, SiO ₂ , Ni	50	yes	97% absorption for ≤ 85	>97.5%	Nano	Yes

Competing interests

The authors declare no competing interests.

Data availability

The datasets used and/or analyzed during the current study are available from the corresponding author on reasonable request.

REFERENCES

- [1] W. Cao, H.-D. Chen, Y.-W. Yu, N. Li, and W.-Q. Chen, "Changing profiles of cancer burden worldwide and in China: a secondary analysis of the global cancer statistics 2020," *Chinese medical journal*, vol. 134, no. 07, pp. 783-791, 2021.
- [2] F. Bray, J. Ferlay, I. Soerjomataram, R. L. Siegel, L. A. Torre, and A. Jemal, "Global cancer statistics 2018: GLOBOCAN estimates of incidence and mortality worldwide for 36 cancers in 185 countries," *CA: a cancer journal for clinicians*, vol. 68, no. 6, pp. 394-424, 2018.
- [3] M. Entezari *et al.*, "Long non-coding RNAs and exosomal lncRNAs: Potential functions in lung cancer progression, drug resistance and tumor microenvironment remodeling," *Biomedicine & Pharmacotherapy*, vol. 150, p. 112963, 2022.
- [4] N. Pashayan and P. D. Pharoah, "The challenge of early detection in cancer," *Science*, vol. 368, no. 6491, pp. 589-590, 2020.
- [5] Y. Van Der Pol and F. Mouliere, "Toward the early detection of cancer by decoding the epigenetic and environmental fingerprints of cell-free DNA," *Cancer cell*, vol. 36, no. 4, pp. 350-368, 2019.
- [6] M. D. A. Paskeh *et al.*, "Emerging role of exosomes in cancer progression and tumor microenvironment remodeling," *Journal of hematology & oncology*, vol. 15, no. 1, p. 83, 2022.
- [7] N. A. Hanjani *et al.*, "Emerging role of exosomes as biomarkers in cancer treatment and diagnosis," *Critical reviews in oncology/hematology*, vol. 169, p. 103565, 2022.
- [8] Q. Maqsood, A. Sumrin, Y. Saleem, A. Wajid, and M. Mahnoor, "Exosomes in Cancer: Diagnostic and Therapeutic Applications," *Clinical Medicine Insights: Oncology*, vol. 18, p. 11795549231215966, 2024.
- [9] S. V. Gaponenko, *Introduction to nanophotonics*. Cambridge University Press, 2010.
- [10] K. W. Mauser *et al.*, "Resonant thermoelectric nanophotonics," *Nature nanotechnology*, vol. 12, no. 8, pp. 770-775, 2017.
- [11] Y. J. Kim, W.-Y. Rho, S.-m. Park, and B.-H. Jun, "Optical nanomaterial-based detection of biomarkers in liquid biopsy," *Journal of Hematology & Oncology*, vol. 17, no. 1, p. 10, 2024.
- [12] A. Kuzin *et al.*, "Real-time surface functionalization of a nanophotonic sensor for liquid biopsy," *Applied Physics Letters*, vol. 123, no. 19, 2023.
- [13] X. Fang, Y. Wang, S. Wang, and B. Liu, "Nanomaterials assisted exosomes isolation and analysis towards liquid biopsy," *Materials Today Bio*, vol. 16, p. 100371, 2022.
- [14] S. Bordy, J. Byun, and L. V. Poulikakos, "Nanophotonic materials: enabling targeted cancer diagnostics and therapeutics with light," *Current Opinion in Chemical Engineering*, vol. 37, p. 100852, 2022.

> REPLACE THIS LINE WITH YOUR MANUSCRIPT ID NUMBER (DOUBLE-CLICK HERE TO EDIT) <

- [15] C. Tan *et al.*, "Cancer Diagnosis Using Terahertz-Graphene-Metasurface-Based Biosensor with Dual-Resonance Response," *Nanomaterials*, vol. 12, no. 21, p. 3889, 2022.
- [16] M. Y. Azab, M. F. O. Hameed, A. M. Nasr, and S. Obayya, "Highly sensitive metamaterial biosensor for cancer early detection," *IEEE Sensors Journal*, vol. 21, no. 6, pp. 7748-7755, 2021.
- [17] M. N. Hamza *et al.*, "Designing a High-sensitivity Microscale Triple-band Biosensor based on Terahertz MTMs to provide a perfect absorber for Non-Melanoma Skin Cancer diagnostic," *IEEE Photonics Journal*, 2024.
- [18] S. K. Patel, J. Surve, and J. Parmar, "Detection of cancer with graphene metasurface-based highly efficient sensors," *Diamond and Related Materials*, vol. 129, p. 109367, 2022.
- [19] M. N. Hamza and M. T. Islam, "Design of MTM-based Multi-band Micro-Biosensor in Terahertz region as perfect absorber for Early-Stage Leukemia Diagnosis with sensitivity 18626373 THz/RIU," *IEEE Sensors Journal*, 2024.
- [20] B. Amini and Z. Atlasbaf, "Design and analysis of high-sensitivity tunable graphene sensors for cancer detection," *Optical and Quantum Electronics*, vol. 55, no. 5, p. 446, 2023.
- [21] M. N. Hamza, S. Koziel, and A. Pietrenko-Dabrowska, "Design and experimental validation of a metamaterial-based sensor for microwave imaging in breast, lung, and brain cancer detection," *Scientific Reports*, vol. 14, no. 1, p. 16177, 2024.
- [22] P. Upender and A. Kumar, "THz dielectric metamaterial sensor with high Q for biosensing applications," *IEEE Sensors Journal*, vol. 23, no. 6, pp. 5737-5744, 2023.
- [23] S. Banerjee, U. Nath, P. Dutta, A. V. Jha, B. Appasani, and N. Bizon, "A theoretical terahertz metamaterial absorber structure with a high quality factor using two circular ring resonators for biomedical sensing," *Inventions*, vol. 6, no. 4, p. 78, 2021.
- [24] Z. Geng, X. Zhang, Z. Fan, X. Lv, and H. Chen, "A route to terahertz metamaterial biosensor integrated with microfluidics for liver cancer biomarker testing in early stage," *Scientific reports*, vol. 7, no. 1, p. 16378, 2017.
- [25] H. E. Nejad, A. Mir, and A. Farmani, "Supersensitive and tunable nano-biosensor for cancer detection," *IEEE Sensors Journal*, vol. 19, no. 13, pp. 4874-4881, 2019.
- [26] M. N. Hamza and M. T. Islam, "Designing an Extremely Tiny Dual-Band Biosensor Based on MTMs in the Terahertz Region as a Perfect Absorber for Non-Melanoma Skin Cancer Diagnostics," *IEEE Access*, vol. 11, pp. 136770-136781, 2023.
- [27] D. Li *et al.*, "Identification of early-stage cervical cancer tissue using metamaterial terahertz biosensor with two resonant absorption frequencies," *IEEE Journal of Selected Topics in Quantum Electronics*, vol. 27, no. 4, pp. 1-7, 2021.
- [28] S. Banerjee, P. Dutta, A. V. Jha, B. Appasani, and M. S. Khan, "A biomedical sensor for detection of cancer cells based on terahertz metamaterial absorber," *IEEE Sensors Letters*, vol. 6, no. 6, pp. 1-4, 2022.
- [29] M. N. Hamza, M. T. Islam, S. Lavadiya, S. Koziel, I. Ud Din, and B. Sanches, "Designing a High-sensitivity Dual-band Nano-Biosensor based on Petahertz MTMs to provide a perfect absorber for Early-Stage Non-Melanoma Skin Cancer diagnostic," *IEEE Sensors Journal*, 2024.
- [30] A. Chaudhuri, B. Rai, and P. Pal, "Design of a dual-band metasurface cross-polarization converter for cancer detection in the terahertz band," *IEEE Sensors Journal*, vol. 24, no. 6, pp. 7292-7298, 2023.
- [31] J. Chen, F. Hu, X. Ma, M. Yang, S. Lin, and A. Su, "Deep neural network assisted terahertz metasurface sensors for the detection of lung cancer biomarkers," *IEEE Sensors Journal*, 2024.
- [32] M. N. Hamza *et al.*, "Development of a Terahertz Metamaterial Micro-Biosensor for Ultrasensitive Multispectral Detection of Early-Stage Cervical Cancer," *IEEE Sensors Journal*, 2024.
- [33] A. Hlali, A. Oueslati, and H. Zairi, "Numerical simulation of tunable terahertz graphene-based sensor for breast tumor detection," *IEEE Sensors Journal*, vol. 21, no. 8, pp. 9844-9851, 2021.
- [34] X. Hou *et al.*, "Cancer biomarkers ultrasensitive detection based on terahertz frequency-comb-like," *IEEE Sensors Journal*, vol. 23, no. 10, pp. 10413-10419, 2023.
- [35] M. N. Hamza *et al.*, "Ultra-compact quintuple-band terahertz metamaterial biosensor for enhanced blood cancer diagnostics," *PLOS ONE*, vol. 20, no. 1, p. e0313874, 2025.
- [36] A. Veeraselvam, G. N. A. Mohammed, K. Savarimuthu, and P. D. Vijayaraman, "An ultra-thin multiband refractive index-based carcinoma sensor using THz radiation," *IEEE Sensors Journal*, vol. 22, no. 3, pp. 2045-2052, 2021.
- [37] D. Xie *et al.*, "Terahertz metamaterial biosensor with double resonant frequencies for specific detection of early-stage hepatocellular carcinoma," *IEEE Sensors Journal*, vol. 23, no. 2, pp. 1124-1131, 2022.
- [38] F. Wahaia *et al.*, "Detection of colon cancer by terahertz techniques," *Journal of Molecular Structure*, vol. 1006, no. 1-3, pp. 77-82, 2011.
- [39] M. N. Hamza *et al.*, "Terahertz Dual-Band Metamaterial Biosensor for Cervical-Cancer Diagnostics," *IEEE Photonics Journal*, 2024.
- [40] M. Rezeg, A. Hlali, and H. Zairi, "THz Biomedical Sensing for Early Cancer Detection: Metamaterial Graphene Biosensors with Rotated Split-Ring Resonators," *IEEE Photonics Journal*, 2024.
- [41] L. Yu *et al.*, "The medical application of terahertz technology in non-invasive detection of cells and tissues: opportunities and challenges," *RSC advances*, vol. 9, no. 17, pp. 9354-9363, 2019.
- [42] M. N. Hamza *et al.*, "Development of a High-Sensitivity Triple-Band Nano-Biosensor Utilizing Petahertz Metamaterials for Optimal Absorption in Early-Stage Leukemia Detection," *IEEE Sensors Journal*, 2025.
- [43] G. Valušis, A. Lisauskas, H. Yuan, W. Knap, and H. G. Roskos, "Roadmap of terahertz imaging 2021," *Sensors*, vol. 21, no. 12, p. 4092, 2021.
- [44] M. N. Hamza, M. T. Islam, and S. Koziel, "Advanced sensor for non-invasive breast cancer and brain cancer

> REPLACE THIS LINE WITH YOUR MANUSCRIPT ID NUMBER (DOUBLE-CLICK HERE TO EDIT) <

- diagnosis using antenna array with metamaterial-based AMC," *Engineering Science and Technology, an International Journal*, vol. 56, p. 101779, 2024.
- [45] W. Zhang *et al.*, "Terahertz metamaterials for biosensing applications: A review," *Biosensors*, vol. 14, no. 1, p. 3, 2023.
- [46] M. N. Hamza *et al.*, "Precision Multi-Band Terahertz Metamaterial Biosensor with Targeted Spectral Selectivity for Early Detection of MCF-7 Breast Cancer Cells," *IEEE Sensors Journal*, 2025.
- [47] Q. Liu *et al.*, "Q-BIC THz Metasurface Biosensor Based on Flexible Polyimide for Solution Detection," *IEEE Sensors Journal*, 2025.
- [48] M. N. Hamza *et al.*, "Design and validation of ultra-compact metamaterial-based biosensor for non-invasive cervical cancer diagnosis in terahertz regime," *PLOS ONE*, vol. 20, no. 2, p. e0311431, 2025.
- [49] L. Shen *et al.*, "Label-Free Detection of Biological Cells Using Quasi-Bound States in the Continuum with Terahertz Metasurface," *IEEE Sensors Journal*, 2025.
- [50] L. Chi *et al.*, "Broadband Infrared to Terahertz detection based on pyramidal polymer-derived ceramic array absorber," *IEEE Sensors Journal*, 2025.
- [51] M. N. Hamza *et al.*, "Polarization-Insensitive Nano-Metamaterial Sensor with Near-Infrared μ and ϵ Negative Properties for Early Cancer Detection via Exosome Analysis (70 THz to 3 PHz)," *IEEE Photonics Journal*, 2025.
- [52] X. Chen, L. Ye, and D. Yu, "Terahertz Hybrid Detection of Chiral Enantiomers with Intrinsic Low Absorption enabled by Metasurface," *IEEE Sensors Journal*, 2025.
- [53] X. You *et al.*, "Ultra-wideband far-infrared absorber based on anisotropically etched doped silicon," *Optics letters*, vol. 45, no. 5, pp. 1196-1199, 2020.
- [54] Y. Cheng and J. Zhao, "Simple design of a six-band terahertz perfect metasurface absorber based on a single resonator structure," *Physica Scripta*, vol. 97, no. 9, p. 095508, 2022.
- [55] Z. Li, Y. Cheng, H. Luo, F. Chen, and X. Li, "Dual-band tunable terahertz perfect absorber based on all-dielectric InSb resonator structure for sensing application," *Journal of Alloys and Compounds*, vol. 925, p. 166617, 2022.
- [56] Y. Cheng, Y. Qian, H. Luo, F. Chen, and Z. Cheng, "Terahertz narrowband perfect metasurface absorber based on micro-ring-shaped GaAs array for enhanced refractive index sensing," *Physica E: Low-dimensional Systems and Nanostructures*, vol. 146, p. 115527, 2023.
- [57] S. Feng *et al.*, "Tri-band terahertz metamaterial absorber based on structural Ti₃C₂T_x MXene for enhanced sensing application," *IEEE Sensors Journal*, 2024.
- [58] C. Rong, B. Cai, Y. Cheng, F. Chen, H. Luo, and X. Li, "Dual-band terahertz chiral metasurface absorber with enhanced circular dichroism based on temperature-tunable InSb for sensing applications," *Physical Chemistry Chemical Physics*, vol. 26, no. 6, pp. 5579-5588, 2024.
- [59] B. Cai, L. Yang, L. Wu, Y. Cheng, and X. Li, "Dual-narrowband terahertz metamaterial absorber based on all-metal vertical ring array for enhanced sensing application," *Physica Scripta*, vol. 99, no. 9, p. 095503, 2024.
- [60] D. M. Mittleman, "Twenty years of terahertz imaging," *Optics express*, vol. 26, no. 8, pp. 9417-9431, 2018.
- [61] H. Tian, G. Huang, F. Xie, W. Fu, and X. Yang, "THz biosensing applications for clinical laboratories: Bottlenecks and strategies," *TrAC Trends in Analytical Chemistry*, vol. 163, p. 117057, 2023.
- [62] M. Gezimati and G. Singh, "Terahertz imaging and sensing for healthcare: current status and future perspectives," *IEEE Access*, vol. 11, pp. 18590-18619, 2023.
- [63] C. Amri, A. K. Shukla, and J.-H. Lee, "Recent advancements in nanoparticle-based optical biosensors for circulating cancer biomarkers," *Materials*, vol. 14, no. 6, p. 1339, 2021.
- [64] D. Chen, B. Xu, Z. Qiu, X. Wang, and J. Wu, "Ultra-broadband terahertz metamaterial absorber based on flexible wave-absorbing material," *Results in Physics*, vol. 52, p. 106880, 2023.
- [65] P. Zhang *et al.*, "Ultra-broadband tunable terahertz metamaterial absorber based on double-layer vanadium dioxide square ring arrays," *Micromachines*, vol. 13, no. 5, p. 669, 2022.
- [66] J. Conde-Vancells *et al.*, "Characterization and comprehensive proteome profiling of exosomes secreted by hepatocytes," *Journal of proteome research*, vol. 7, no. 12, pp. 5157-5166, 2008.
- [67] M.-P. Caby, D. Lankar, C. Vincendeau-Scherrer, G. Raposo, and C. Bonnerot, "Exosomal-like vesicles are present in human blood plasma," *International immunology*, vol. 17, no. 7, pp. 879-887, 2005.
- [68] J. M. Street *et al.*, "Identification and proteomic profiling of exosomes in human cerebrospinal fluid," *Journal of translational medicine*, vol. 10, pp. 1-7, 2012.
- [69] C. Théry, S. Amigorena, G. Raposo, and A. Clayton, "Isolation and characterization of exosomes from cell culture supernatants and biological fluids," *Current protocols in cell biology*, vol. 30, no. 1, pp. 3.22. 1-3.22. 29, 2006.
- [70] C. Gabriel, S. Gabriel, and Y. Corthout, "The dielectric properties of biological tissues: I. Literature survey," *Physics in medicine & biology*, vol. 41, no. 11, p. 2231, 1996.
- [71] B. S. Chia, Y. P. Low, Q. Wang, P. Li, and Z. Gao, "Advances in exosome quantification techniques," *TrAC Trends in Analytical Chemistry*, vol. 86, pp. 93-106, 2017.
- [72] H. Chen, T. Yamakawa, M. Inaba, M. Nakano, and J. Suehiro, "Characterization of extra-cellular vesicle dielectrophoresis and estimation of its electric properties," *Sensors*, vol. 22, no. 9, p. 3279, 2022.
- [73] D. Yu *et al.*, "Exosomes as a new frontier of cancer liquid biopsy," *Molecular cancer*, vol. 21, no. 1, p. 56, 2022.
- [74] C. Gardiner *et al.*, "Measurement of refractive index by nanoparticle tracking analysis reveals heterogeneity in extracellular vesicles," *Journal of extracellular vesicles*, vol. 3, no. 1, p. 25361, 2014.
- [75] E. Van Der Pol, A. Hoekstra, A. Sturk, C. Otto, T. Van Leeuwen, and R. Nieuwland, "Optical and non-optical methods for detection and characterization of

> REPLACE THIS LINE WITH YOUR MANUSCRIPT ID NUMBER (DOUBLE-CLICK HERE TO EDIT) <

- microparticles and exosomes," *Journal of Thrombosis and Haemostasis*, vol. 8, no. 12, pp. 2596-2607, 2010.
- [76] Y. Zhang, L. Shi, and L. Esfandiari, "Biophysical Characterization of Exosomes Based on their Unique Dielectric Properties," *Biophysical Journal*, vol. 118, no. 3, p. 175a, 2020.
- [77] H. Altug, S.-H. Oh, S. A. Maier, and J. Homola, "Advances and applications of nanophotonic biosensors," *Nature nanotechnology*, vol. 17, no. 1, pp. 5-16, 2022.
- [78] M. A. Habib, M. S. Anower, and M. N. Islam, "Terahertz sensing based on photonic crystal fibers," *Terahertz Technology*, p. 109, 2022.
- [79] Y. Yang, Y. Xiang, and X. Qi, "Design of photonic crystal biosensors for cancer cell detection," *Micromachines*, vol. 14, no. 7, p. 1478, 2023.
- [80] X. Yang *et al.*, "Biomedical applications of terahertz spectroscopy and imaging," *Trends in biotechnology*, vol. 34, no. 10, pp. 810-824, 2016.
- [81] M. G. Blevins, A. Fernandez-Galiana, M. J. Hooper, and S. V. Boriskina, "Roadmap on universal photonic biosensors for real-time detection of emerging pathogens," in *Photonics*, 2021, vol. 8, no. 8, p. 342: Multidisciplinary Digital Publishing Institute.
- [82] J. Mejía-Salazar and O. N. Oliveira Jr, "Plasmonic biosensing: Focus review," *Chemical reviews*, vol. 118, no. 20, pp. 10617-10625, 2018.
- [83] C. Liang *et al.*, "Tunable triple-band graphene refractive index sensor with good angle-polarization tolerance," *Optics Communications*, vol. 436, pp. 57-62, 2019.
- [84] C. Gandhi, P. R. Babu, and K. Senthilnathan, "Ultra-thin polarization independent broadband terahertz metamaterial absorber," *Frontiers of Optoelectronics*, vol. 14, no. 3, pp. 288-297, 2021.
- [85] Z. Zheng *et al.*, "Terahertz perfect absorber based on flexible active switching of ultra-broadband and ultra-narrowband," *Optics Express*, vol. 29, no. 26, pp. 42787-42799, 2021.
- [86] Y. Li *et al.*, "Tunable ultra-broadband terahertz perfect absorber based on vanadium oxide metamaterial," *Optics Express*, vol. 29, no. 25, pp. 41222-41233, 2021.
- [87] G. Wu, X. Jiao, Y. Wang, Z. Zhao, Y. Wang, and J. Liu, "Ultra-wideband tunable metamaterial perfect absorber based on vanadium dioxide," *Optics Express*, vol. 29, no. 2, pp. 2703-2711, 2021.
- [88] M. Fu, J. Wang, S. Guo, Z. Wang, P. Yang, and Y. Niu, "A polarization-insensitive broadband terahertz absorber using patterned graphene," *Nanomaterials*, vol. 12, no. 21, p. 3763, 2022.
- [89] S. Hafeez, J. Yu, F. A. Umrani, A. Majeed, and W. Yun, "A Broadband Meta-Absorber for Curved Terahertz Stealth Applications," *Electronics*, vol. 13, no. 15, p. 2966, 2024.
- [90] Z. Chen *et al.*, "Graphene Multi-Frequency Broadband and Ultra-Broadband Terahertz Absorber Based on Surface Plasmon Resonance," *Electronics*, vol. 12, no. 12, p. 2655, 2023.
- [91] X. Wang, G. Wu, Y. Wang, and J. Liu, "Terahertz broadband adjustable absorber based on VO₂ multiple ring structure," *Applied Sciences*, vol. 13, no. 1, p. 252, 2022.
- [92] U. U. R. Qureshi, M. I. Khan, and B. Hu, "A theoretical proposal for an actively controlled ultra-wideband absorber based on vanadium dioxide hybrid metamaterials," *Applied Sciences*, vol. 12, no. 19, p. 10164, 2022.